Electronic Supplementary Material (ESI) for Energy & Environmental Science.

Supplementary Information

Boosting Solar Water Oxidation Performance of $BiVO_4$ Photoanode by Crystallographic Orientation Control

Hyun Soo Han[a], Sun Shin[b], Dong Hoe Kim[b], Ik Jae Park[b], Ju Seong Kim[b], Po-Shun Huang[c], Jung-Kun Lee[c], In Sun Cho[d]*, and Xiaolin Zheng[a]*

[a]Department of Mechanical Engineering, Stanford University, Stanford, CA 94305, USA.

[b]Department of Materials Science and Engineering, Seoul National University, Seoul, Korea.

[c]Department of Mechanical Engineering and Materials Science, University of Pittsburgh, Pittsburgh, PA 15261, USA.

[d]Department of Materials Science & Engineering, and Energy Systems Research, Ajou University, Suwon, Korea.

* Corresponding authors: insuncho@ajou.ac.kr, xlzheng@stanford.edu

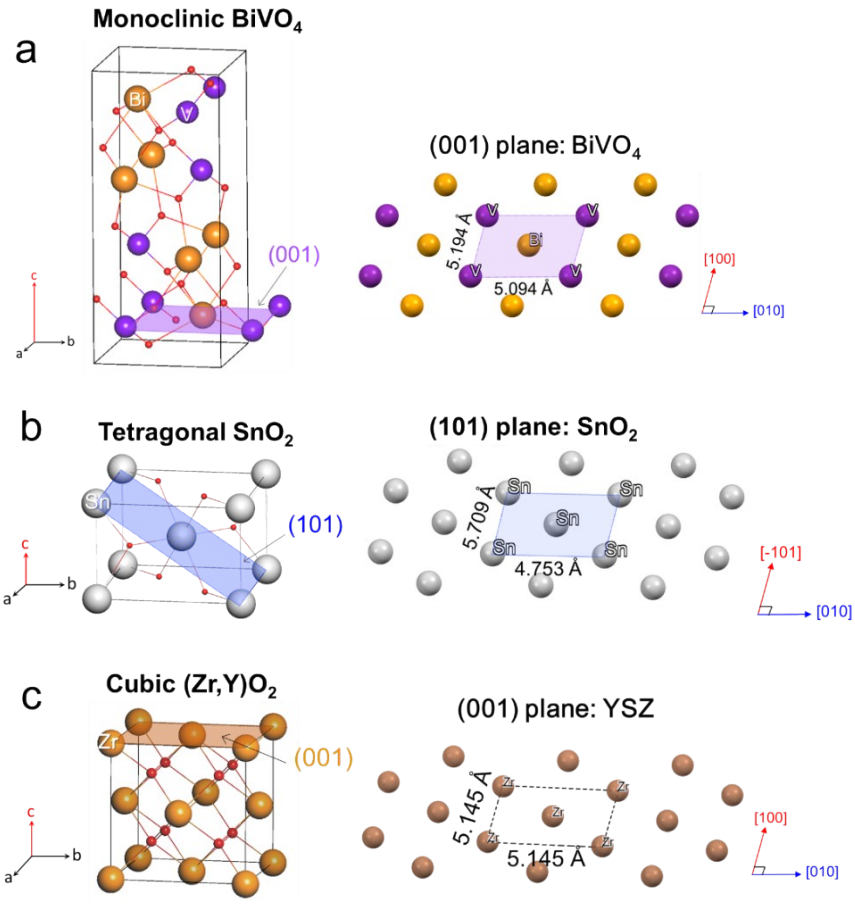

d

Substrate	Crystal system	a (Å)	b (Å)	c (Å)	β (°)	Lattice mismatch (%)		
						$[100]_{BVO}$ || $[100]_{SUB}$	$[010]_{BVO}$ || $[010]_{SUB}$	$[100]_{BVO}$ || $[-101]_{SUB}$
BVO	Monoclinic	5.194	5.094	11.697	90.387	-	-	-
YSZ	Cubic	5.145	5.145	5.145	90	1.0	1.0	-
FTO (SnO_2:F)	Tetragonal	4.738	4.738	3.188	90	-	6.7	9.9
TiO_2	Tetragonal	4.593	4.593	2.958	90	-	9.8	5.2

Fig. S1 (a) Monoclinic unit cell of $BiVO_4$ and atomic arrangement of $BiVO_4$ (00l) plane. (b) Tetragonal unit cell of rutile SnO_2 and atomic arrangement of SnO_2 (101) plane. (c) Cubic unit cell of $(Zr,Y)O_2$ (YSZ) and atomic arrangement of YSZ (001) plane. The atomic arrangements of both the $BiVO_4$ (001) and SnO_2 (101) planes are identical and the lattice mismatch values in $[010]_{BiVO4}//[010]_{SnO2}$ and $[100]_{BiVO4}//[-101]_{SnO2}$ are 7.2 % and 9.0 % respectively. (d) Crystal structures, lattice parameters and lattice mismatch values of $BiVO_4$, YSZ, FTO, and TiO_2. Atomic configurations of BVO (001) plane are well-matched not only to YSZ (001) plane but also to SnO_2 (101) and TiO_2 (101) planes.

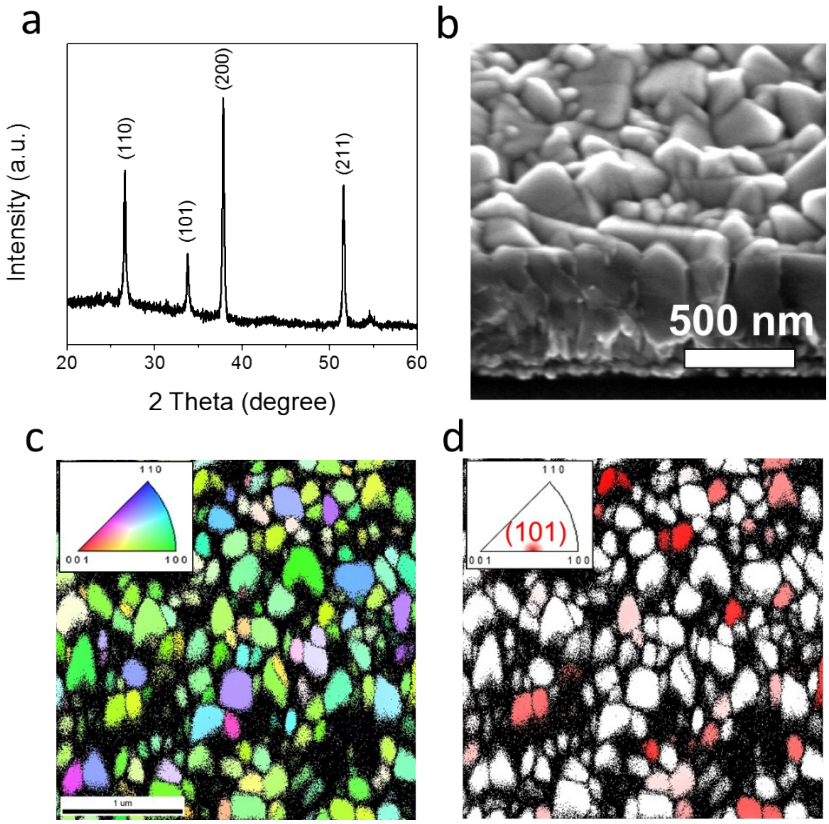

Fig. S2 Distribution of {101} facets in bare FTO/glass substrate (Pilkington, TEC8).
(a) Typical XRD pattern, (b) SEM image and (c, d) Inverse pole figure (grain orientation) maps of the FTO/glass substrate. Approximately 10 % of surface-area in the FTO/glass substrate are exposed with {101} plane.

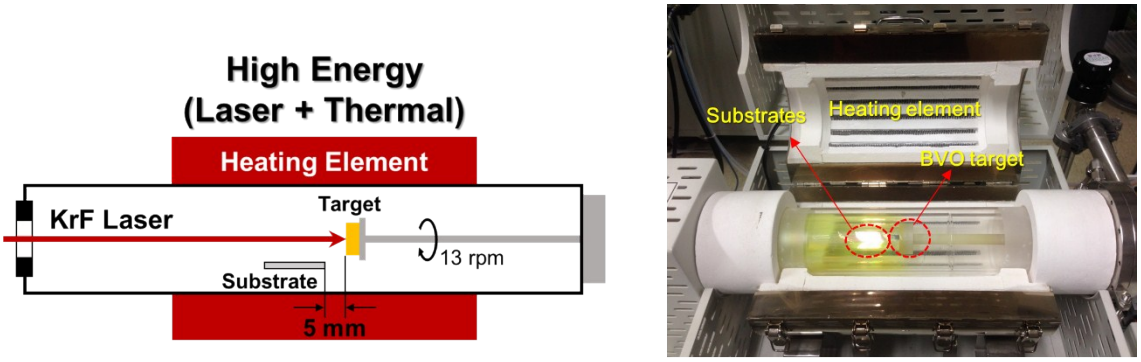

Experimental variables:

- Laser power: 0.8, 1.0, 1.5 J/cm^2
- Growth temperature: 25, 200, 300, 500 ^{o}C
- Growth time: 5, 15, 30, 60 min
- O_2 partial pressure: 100, 300, 500, 800 mTorr
- Position of substrates: 5 mm away from the BVO target

Fig. S3 Laser ablation system and experimental variables. Compared to the sol-gel drop casting method, laser ablation method has a lot of advantages in sample preparation. This system is able to control the variables during the synthesis such as temperature, type of reactive gas and its pressure, which enables to grow epitaxial films, synthesize various morphologies, compositions and phases of sample. High energy excimer laser (KrF, 248 nm, 5 Hz) ablates the BVO target and creates a plasma plum composed of the ablated BVO clusters, then the ablated BVO clusters are deposited on the FTO/glass substrate for which a high thermal energy is supplied to provide enough energy for the epitaxial growth. Laser power, O_2 partial pressure, growth temperature and time were controlled to deposit the $BiVO_4$ photoanode on various substrates (FTO, ITO, Ti metal, TiO_2 single crystal wafers). We confirmed that growth temperature is the most critical factor to grow the [001] preferentially-oriented $BiVO_4$ on FTO/glass substrate.

Optimization of laser ablation deposition conditions for the epitaxial growth of $BiVO_4$ on FTO/glass substrates.

1. **Control of growth temperature (200, 300 and 500 °C)**

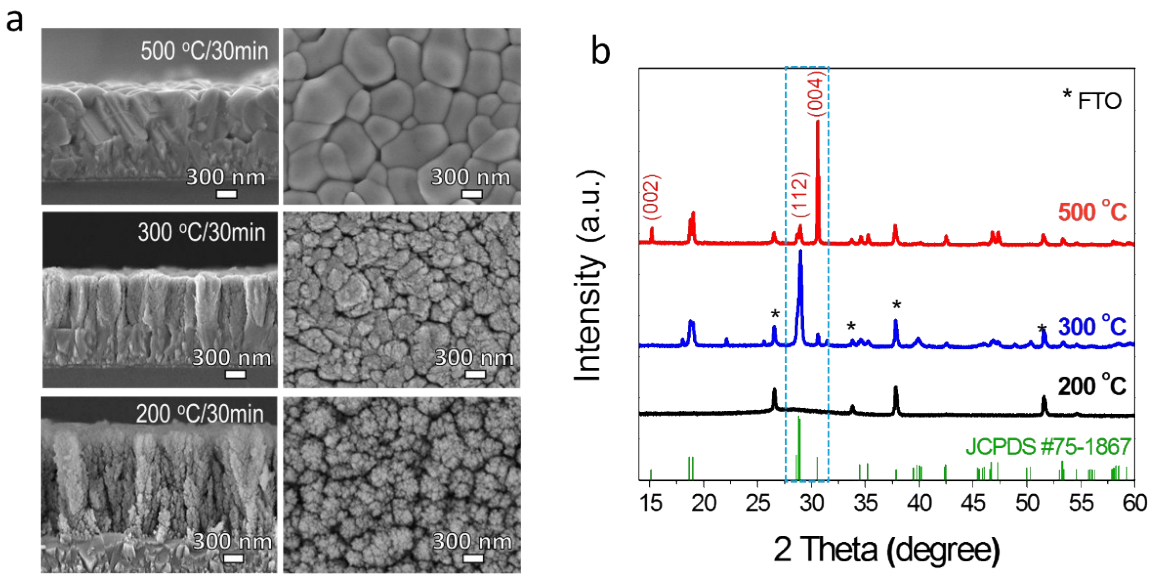

Fig. S4 Effects of growth temperature on morphology and crystal structure of the BVO grown on the FTO/glass substrates. (a) Cross-sectional and top view SEM images and (b) XRD patterns of the BVO grown on FTO/glass substrates. O_2 partial pressure = 300 mTorr, growth time = 30 min. Film thickness: ~800 nm (500 °C/30min), ~900 nm (300°C/30min), 1,700 nm (200 °C/30min). At 200 °C: amorphous & hierarchical nanostructure, at 300 °C: crystalline & columnar nanostructure, at 500°C: Crystalline, (00l)-textured BVO film with micro-sized grains. To grow the [001] preferentially-oriented BVO on FTO/glass substrate, a growth temperature above 500 °C is required.

2. Control of oxygen partial pressure (100, 300, 500 and 800 mTorr)

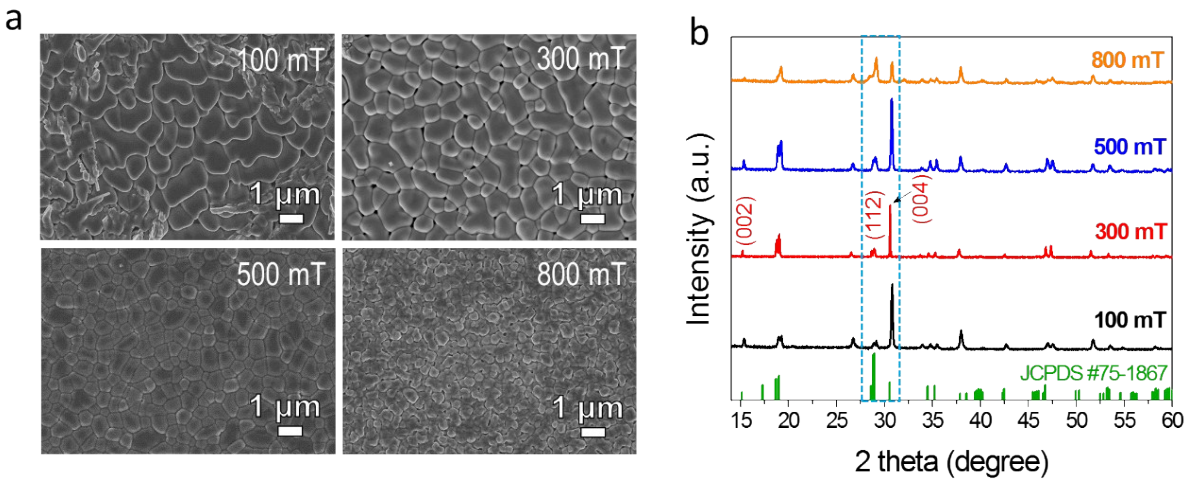

Fig. S5 Effects of oxygen partial pressure on growth morphology and crystal structure of the BVO grown on the FTO/glass substrates. (a) Top-view SEM images and (b) XRD patterns of BVO grown on FTO/glass substrates. Growth temperature = 500 °C. Growth time = 30 min. Film thickness: ~ 800 nm. The O_2 partial pressure has little impact on the [001] preferentially-oriented BVO film on FTO/glass substrates when the growth temperature is 500 °C.

3. Control of laser powder (0.8, 1.0 and 1.5 J/cm^2)

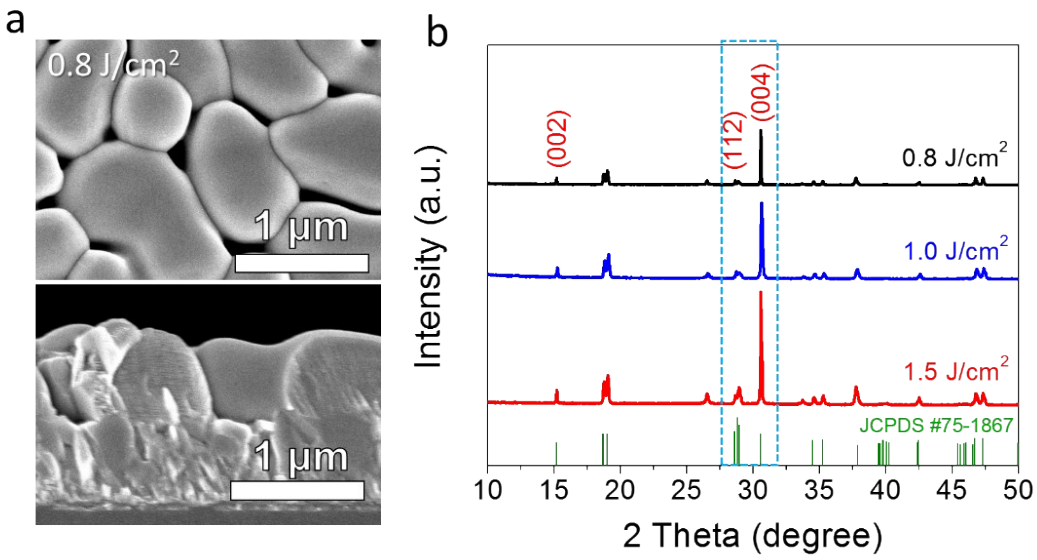

Fig. S6 Effects of laser power density on growth morphology and crystal structure of the BVO on FTO/glass substrates. (a) Top-view and cross-sectional SEM images of BVO grown on FTO/glass substrate by using the laser powder density of 0.8 J/cm^2. (b) XRD patterns of the BVO grown on the FTO/glass substrates using different laser powder density. (Growth temperature = 500 ^{o}C, growth time = 30 min, O_2 partial pressure = 300 mTorr). The laser power density has little impact on the growth morphology and crystal structure of the BVO on the FTO/glass substrates when the growth temperature is 500 ^{o}C.

4. Control of growth time (5, 15, 30, and 60 min @ 500 °C)

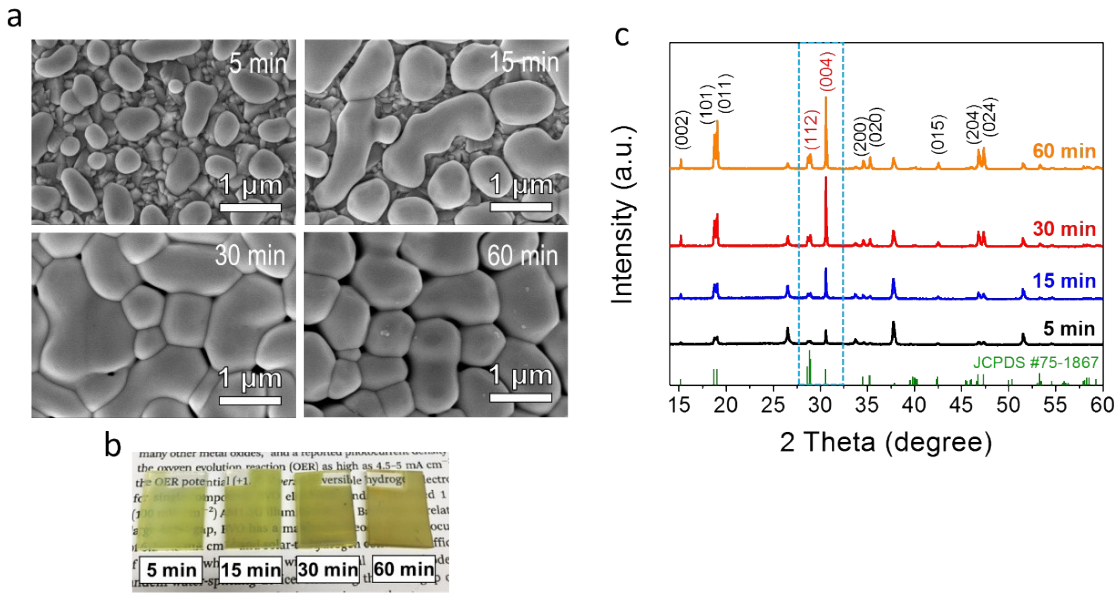

Fig. S7 Effects of growth time on morphology and crystal structure of the BVO grown on the FTO/glass substrates. (a) Top-view SEM images and (b) corresponding sample photographs, (c) XRD patterns of the BVO grown on FTO/glass substrates. Growth temperature = 500 °C. O_2 partial pressure = 300 mTorr. Film thickness: ~200 nm (5min), ~500 nm (15min), ~800 nm (30min), 1,500 nm (60min). The results show that the p-BVO grows at a specific points/grains on the FTO surface, which suggests a Volmer-Weber (*i.e.*, 3D Island) type epitaxial growth process.

Sol-gel deposition (drop-casting) of randomly-oriented $BiVO_4$ on FTO/glass substrates.

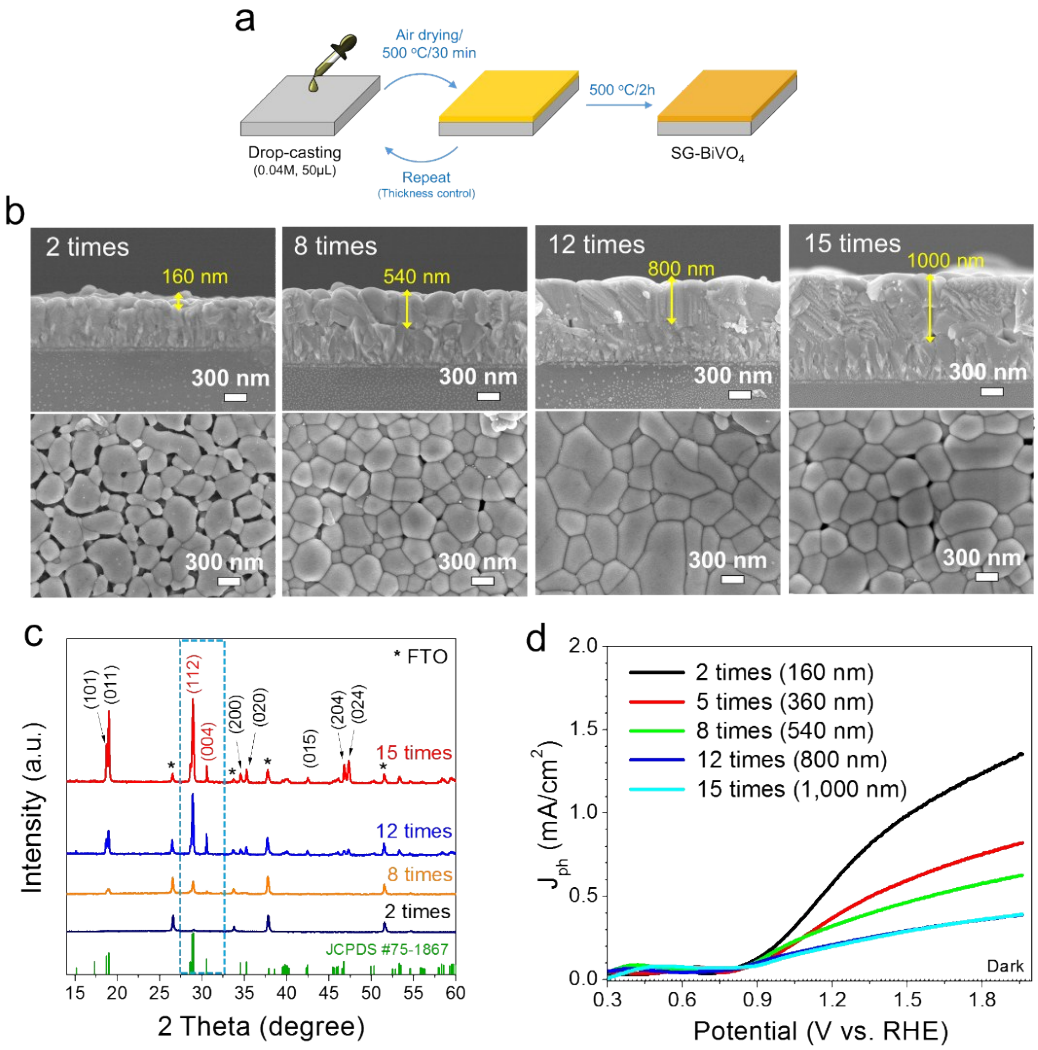

Fig. S8 Modified Sol-gel deposition of randomly-oriented BVO (r-BVO) on the FTO/glass substrates. (a) Schematic process of the sol-gel drop-casting method. (b) Cross-sectional and top view SEM images and (c) XRD patterns and (d) PEC J-V curves of the r-BVO deposited on FTO/glass substrates. In order to grow larger grains (~1 μm) that is comparable to the p-BVO, an intermediate annealing temperature of 500 °C was used. Film thickness: ~70 nm/cycles (2 times = 160 nm, 8 times = 540 nm, 12 times = 800 nm, 15 times=1,000 nm). Unlike the p-BVO, the r-BVO exhibited diverse XRD diffraction peaks (no preferred orientation), *i.e.*, random-oriented grains on FTO/glass substrates are formed. For the PEC J-V measurements, a phosphate buffer electrolyte (pH 7.0), simulated solar light (AM1.5G, 100 mW/cm^2) and three electrode system were used.

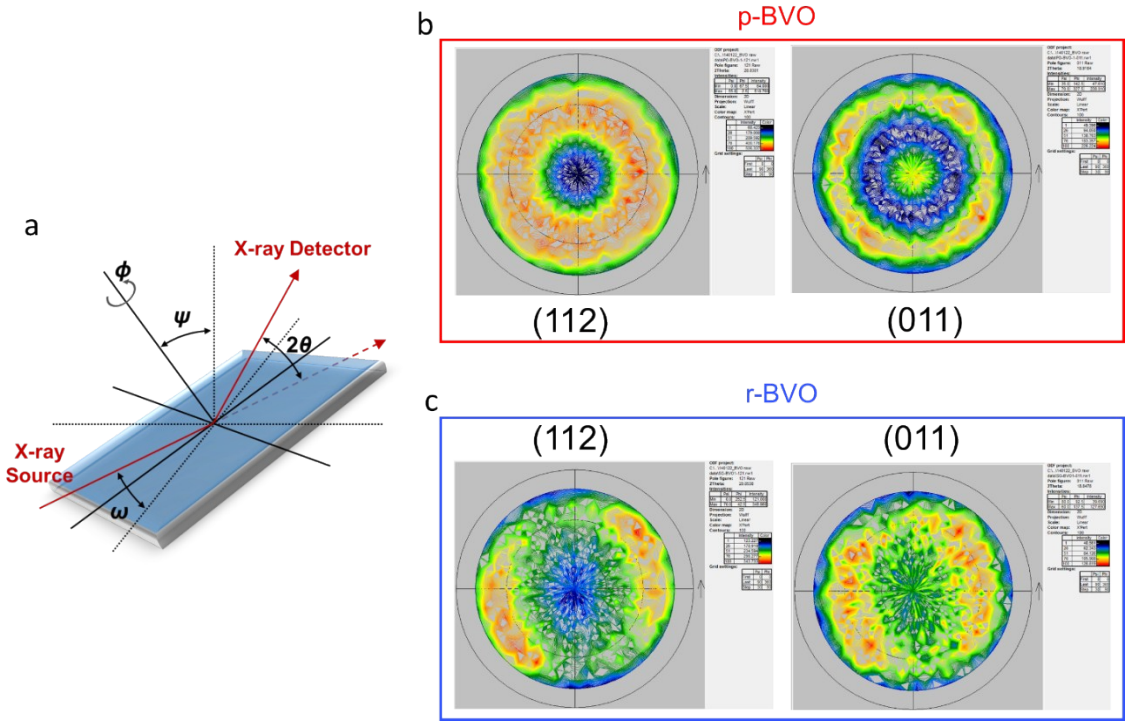

Fig. S9 (112) and (011) pole figure maps of the p-BVO and r-BVO photoanode grown on FTO substrates. Pole figure is an X-ray diffraction method for obtaining crystal in-plane orientation information. The X-ray and detector positions (θ-2θ) are fixed on a certain crystalline plane. Then the sample is rotated to $\phi = 0 - 360^{o}$ with changing the tilt φ of the crystalline plane. (a) Schematic drawing of the pole figure measurement. The (112) and (011) pole figure maps of (b) the p-BVO and (c) r-BVO. The results show that the p-BVO has a [00l] out-of-plane orientation and random in-plane orientation, while the r-BVO has a random out-of-plane and in-plane orientations.

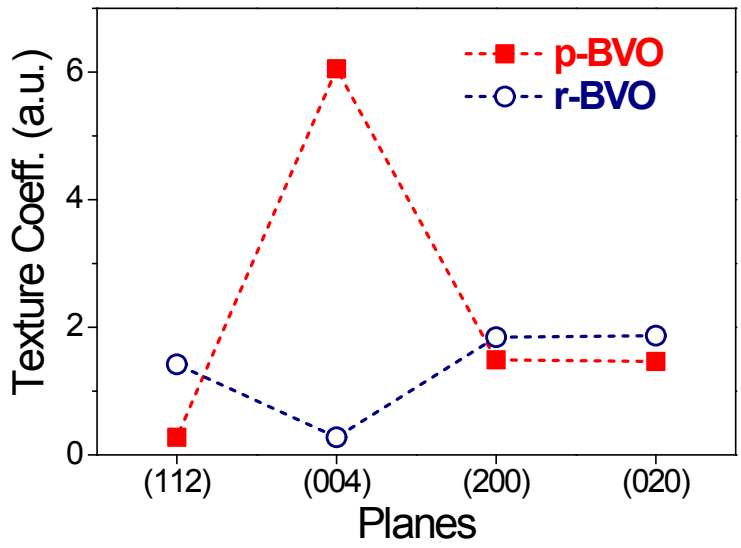

Fig. S10 Texture coefficient of p-BVO and r-BVO. The texture coefficient (*P*) was calculated from the XRD data in figure 2c using the following equation:

$$P_{(hkl)} = \frac{I_{(hkl)} \, \Sigma I_{0,(hkl)}}{I_{0,(hkl)} \, \Sigma I_{(hkl)}}$$

, where $I_{(hkl)}$ is the measured peak intensity of the (*hkl*) plane, $I_{0,(hkl)}$ is the standard intensity from JCPDS card (#75-1867). For randomly oriented film, *P* equals 1. When *P* is greater than 1 for a specific plane, it indicates that the crystal has a preferential growth direction perpendicular to that plane.

Crystal quality investigation

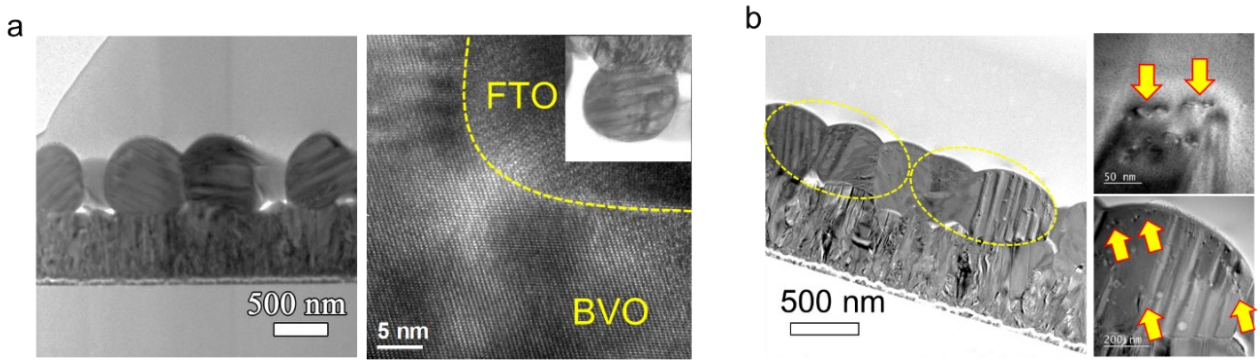

Fig. S11 Investigation of crystal quality (*i.e.*, defect density). TEM images of (a) p-BVO/FTO, and (c) r-BVO/FTO. Comparing to the p-BVO (smooth and continuous cross-section), the r-BVO shows a large number of point or line defects due to its layer-by-layer spin-coating/annealing method, which might induce a stacking faults or interfacial inhomogeneity.

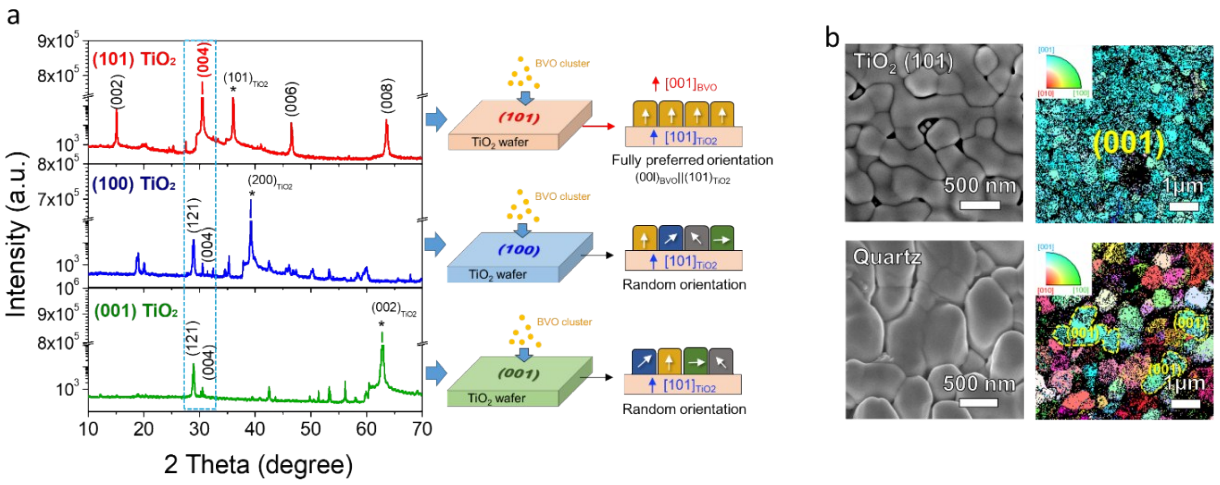

Fig. S12 Growth of the BVO on single-crystal rutile-TiO_2 wafers with different orientations, *i.e.*, (101), (100) and (001) TiO_2. (a) XRD patterns of the BVO grown on the (101), (100) and (001) TiO_2 wafers (growth temperature = 500 °C, growth time = 30 min, O_2 partial pressure = 300 mTorr). Only (101) TiO_2 wafer produces fully [00l] preferentially-oriented BVO film, confirming the epitaxial growth of the BVO on the (101) TiO_2 substrate due to the epitaxial matching, *i.e.*, identical atomic arrangements in between the BVO (00l) and TiO_2 (101) planes: epitaxial relationship of $(001)_{BVO}||(101)_{TiO2\ or\ FTO}$. (b) Top-view SEM and EBSD (grain orientation) mapping images of the BVO/(101)TiO_2 and BVO/quartz samples, showing that the BVO grown on (101) TiO_2 substrate is fully oriented into the [001] direction, while the quartz substrate produces a randomly-oriented BVO. The results show that the choice of the substrate is critical for the growth of p-BVO.

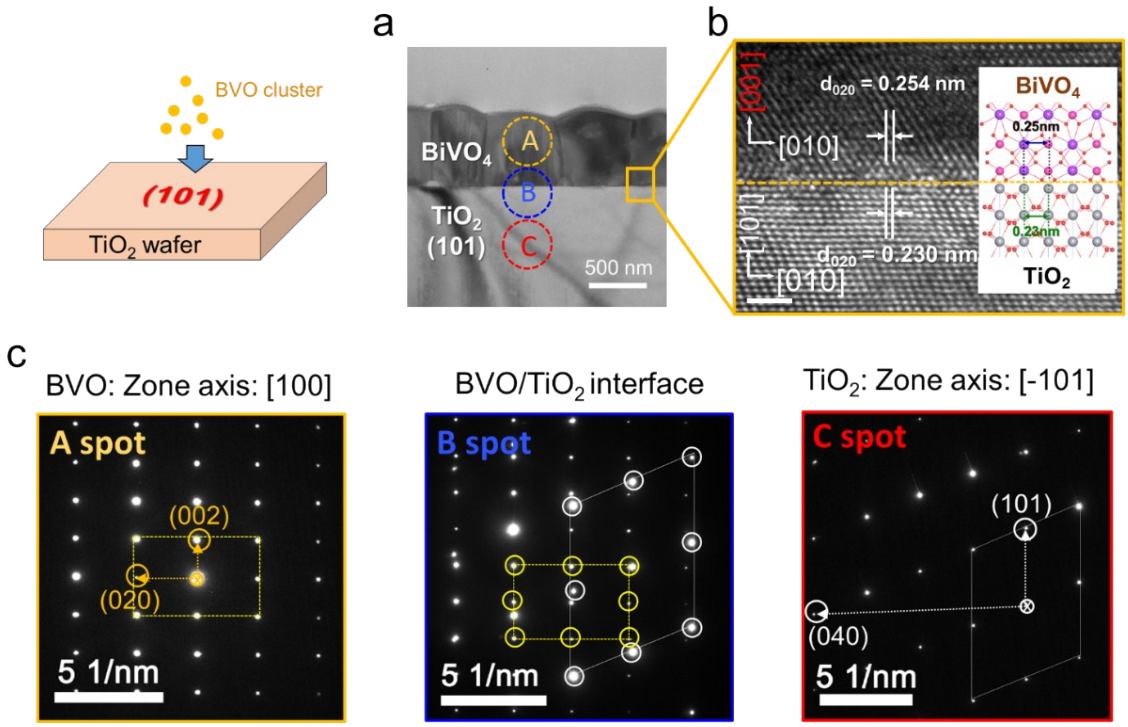

Fig. S13 Identification of epitaxial relationship between the p-BVO and (101) TiO_2 substrate. (a) Cross-sectional TEM and (b) high-resolution TEM images of the p-BVO/(101) TiO_2 substrate, scale bar: 3 nm. The inset shows a model of the expected epitaxial alignment between BVO (020) and TiO_2 (020) planes. (c) Selected area electron diffraction (SAED) patterns at spots of A, B, and C from Fig. S12a. This result confirms the epitaxial growth of the p-BVO on (101) TiO_2 (or SnO_2) substrate with an epitaxial relationship of BVO (00l)//TiO_2 (101).

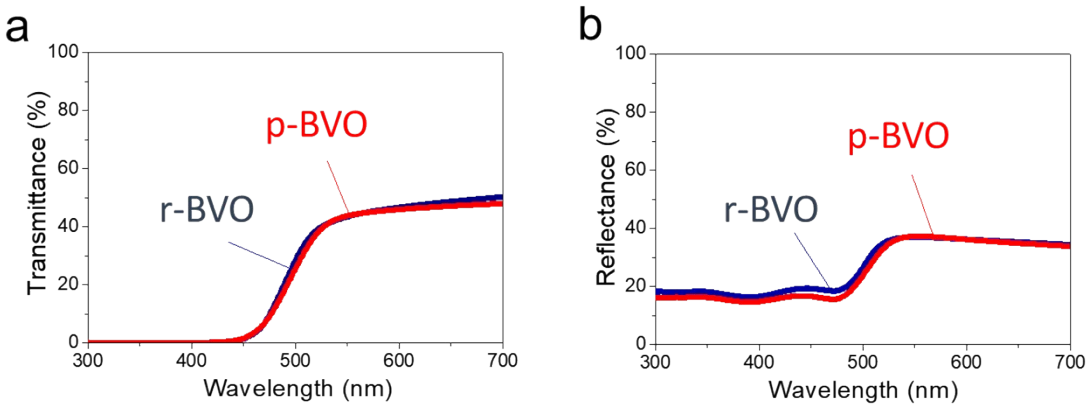

Fig. S14 (a) Transmittance and (b) Reflectance spectra of the p-BVO and r-BVO (film thickness: ~800 nm) over a wavelength range of 300-700 nm. Although the r-BVO shows slightly higher reflectance than the p-BVO due to its denser morphology, no big differences in transmittance and reflectance are observed, *i.e.*, both the p-BVO and r-BVO shows comparable light absorption.

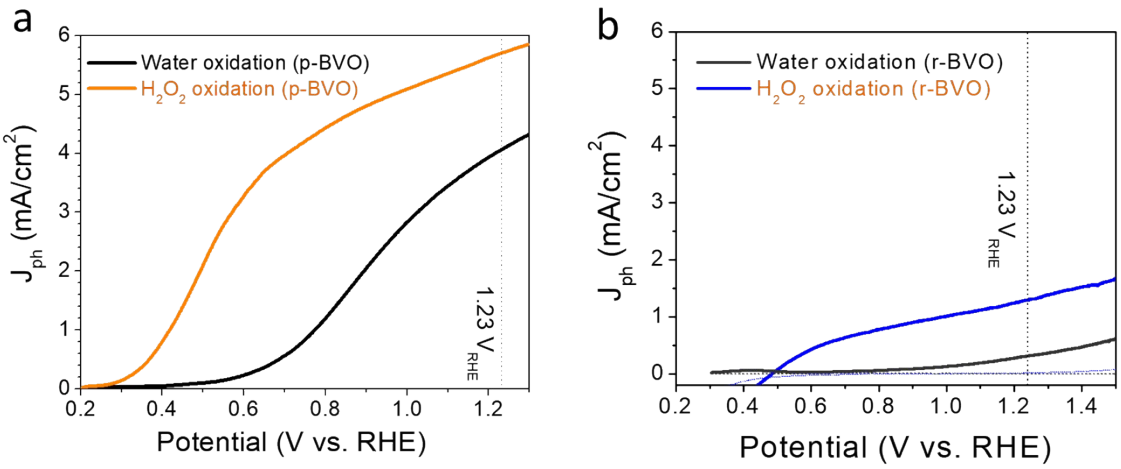

Fig. S15 Charge transfer efficiency measurements. J-V curves of (a) p-BVO and (b) r-BVO under water and H_2O_2 oxidation conditions. The charge transport and transfer efficiencies were estimated as functions of applied potential by using H_2O_2 as a hole scavenger under AM1.5G simulated solar light illumination. The key assumption for this approach is that the oxidation kinetics of H_2O_2 is very fast and its charge transfer efficiency is 100 %, so the ratio of photocurrent density measured in H_2O and H_2O_2 give the charge transfer efficiency ($\eta_{transfer}$) for H_2O. (Eq. 1) The charge transport efficiency ($\eta_{transport}$) was further calculated by dividing photocurrent density in H_2O_2 by the total light absorption efficiency (J_{abs}) which is obtained from integration of light absorption with respect to the AM1.5G solar light spectrum (Eq. 2).

$$\text{Charge transfer efficiency } (\eta_{transfer}) = J_{ph,water}/J_{ph,H2O2} \times 100\ (\%) \qquad (1)$$

$$\text{Charge transport efficiency } (\eta_{transport}) = J_{ph,H2O2}/J_{abs} \qquad (2)$$

Exposed facets and their impact for PEC water oxidation

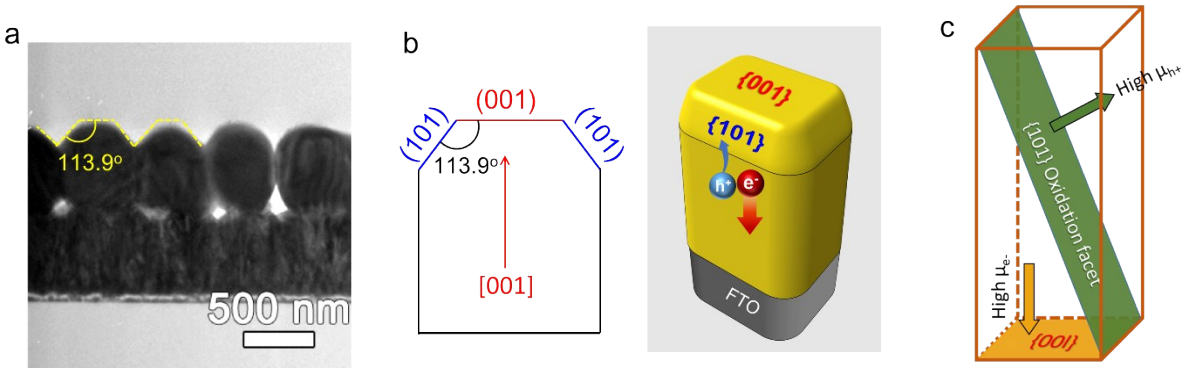

Fig. S16 Exposed surface facets of the p-BVO grown on the FTO/glass substrate. (a) Cross-sectional TEM image. (b) Schematic drawing of the exposed surface facets in the (00l)-textured BVO grain, *i.e.*, dual facets of {001} and {101}. (c) Functions of the dual facets. Previous experimental and theoretical studies have shown that the (00l) facet have much higher OER activity and also the dual facets enable a spatial charge separation, thereby improving charge separation and transport efficiencies for PEC water oxidation.

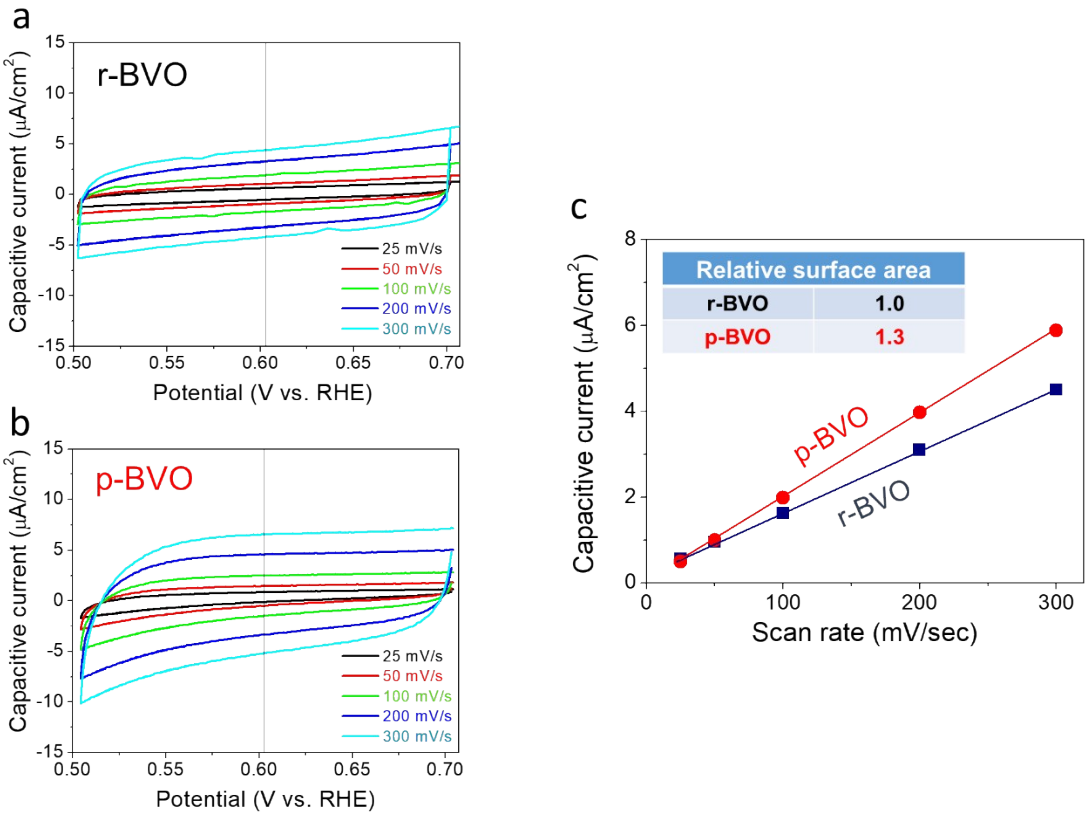

Fig. S17 Electrochemical active surface area (ECSA) measurements. (a) Cyclic voltammetry (C-V) curves of the p-BVO and r-BVO photoanodes measured at different scan rates (25-300 mV/sec). The sweep potential range, *i.e.*, (-0.12 - 0.08 V vs. Ag/AgCl → 0.5 - 0.7 V vs. RHE) was selected. In this range, all current is only attributed to capacitive charging due to the absence of any redox features in the dark condition. Even though it is not possible to obtain a value of the true electrochemical surface area per projected geometric area without an atomically flat $BiVO_4$ reference standard and detailed knowledge of the electronically accessible surface sites, we adopted this method and determined the relative electrochemical surface area by assuming that the intrinsic specific surface capacitance of all $BiVO_4$ films is approximately the same.

a

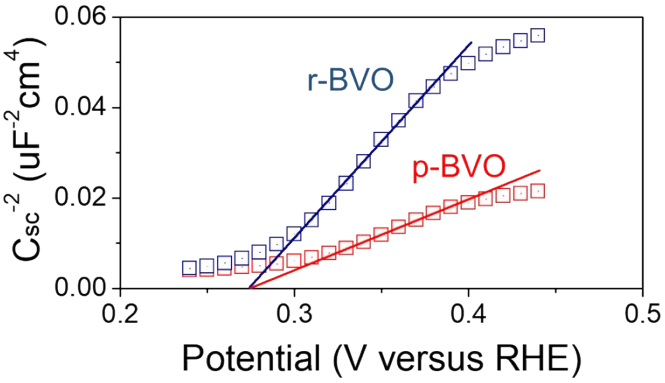

b

	V_{fb} (flat band potential)	N_D (Carrier density, cm^{-1})
p-BVO	~0.27 V_{RHE}	~8.4 x 10^{19}
r-BVO	~0.27 V_{RHE}	~3.0 x 10^{19}

Fig. S18 Mott-Schottky analysis. (a) Mott-Schottky plots of the p-BVO and r-BVO photoanode. (b) Summary of the estimated flat band potential (V_{fb}) and charge carrier density (N_D) values. Both p-BVO and r-BVO show comparable flat band potential values (~0.27 V vs. RHE). However, the p-BVO exhibits two times larger N_D than the r-BVO, which is attributed that the p-BVO is synthesized in relatively oxygen-deficient atmosphere and which can generate oxygen vacancies.

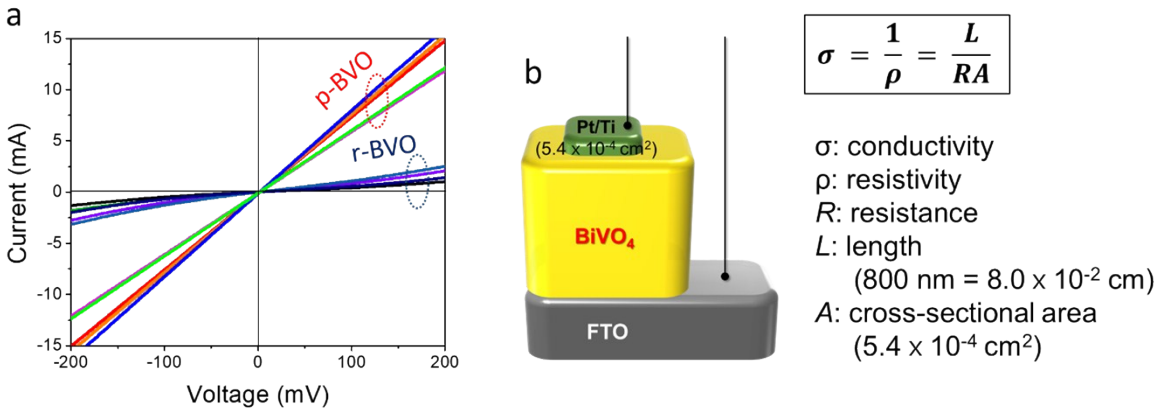

$$\sigma = \frac{1}{\rho} = \frac{L}{RA}$$

c

Sample	Conductivity (S/cm)	e⁻ mobility (Cm²/V-sec)
p-BVO	0.0103 ± 0.0017	0.0008 ± 0.0001
r-BVO	0.0015 ± 0.0007	0.0003 ± 0.0001

Fig. S19 Electrical resistivity (conductivity) measurements of the p-BVO and r-BVO photoanodes. (a) Current-voltage (I-V) curves. Five different positions are measured. (b) Schematic drawing for the I-V measurement. (c) Summary of estimated conductivity and electron mobility values. Charge carrier densities measured by the Mott-Schottky analysis are used for the mobility calculation. The p-BVO shows ~9 times larger conductivity and ~2 times higher e^- mobility.

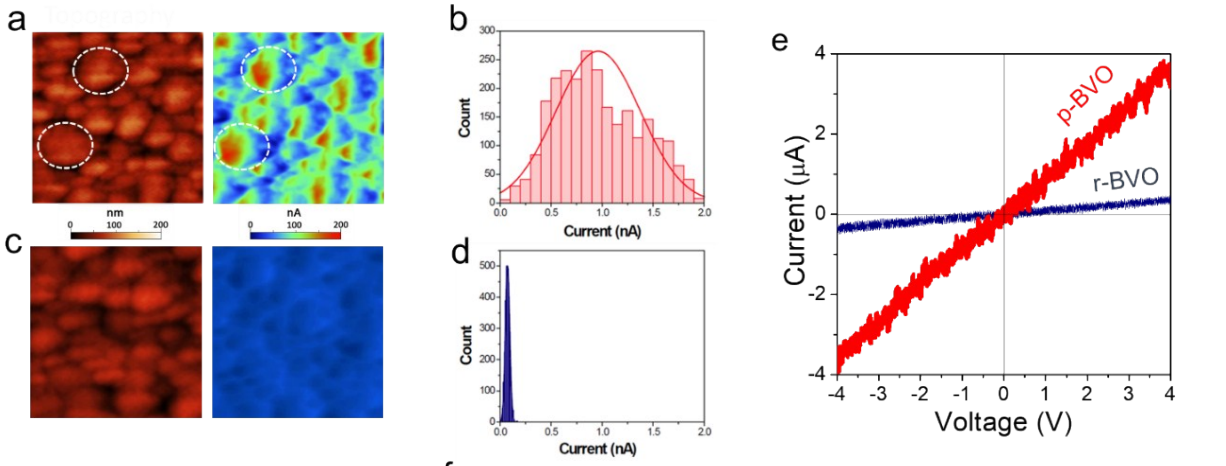

f

Samples	Average J_{av} (mA/cm^2)	Resistance (MOhm)
p-BVO	0.886 ± 0.034	~1.12
r-BVO	0.068 ± 0.002	11.49

Fig. S20 Conductive atomic force microscopy (c-AFM) analysis of the p-BVO and r-BVO photoanodes. (a) Topography, current map and (b) current distribution of the p-BVO photoanode. (c) Topography, current map and (d) current distribution of the r-BVO photoanode. (e) Representative I-V characteristics. (f) Summary of average current density and resistance values. The p-BVO shows ~10 times lower resistance values, which is in good agreement with the electrical resistivity measurements results (Fig. S18). Additionally, as shown by the dotted-circles in Fig. S19a, the (001) facet area (near center of a grain) show much larger current than the (101) facet region (near edge of a grain) for the p-BVO, indicating accumulation of electrons at the (00l) facet, *i.e.*, fast transport of electrons along [00l] direction in the p-BVO.

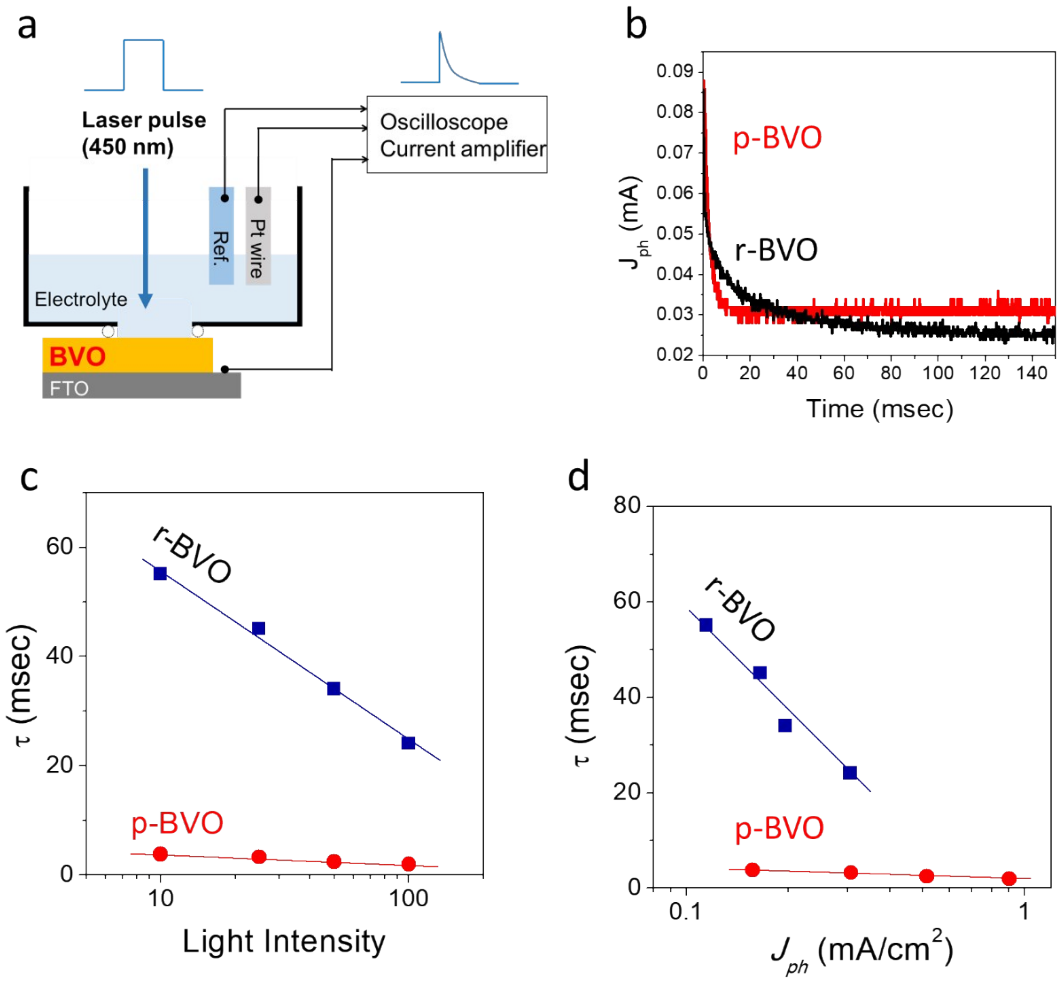

Fig. S21 Charge transport time measurement of the p-BVO and r-BVO (film thickness: 800 nm) at the working condition: Stepped light-induced transient measurement of photocurrent (SLIM-PC) method. (a) Measurement setup. (b) Photocurrent decay curves. (c) Charge transport time vs. light intensity. (d) Charge transport time vs. photocurrent density value. The photocurrent in the three electrode system was measured at a short-circuit condition under illumination of 450 nm diode layer (impinging light was modulated by connecting a function generator). The photocurrent transient was measured by using an oscilloscope (Tektronix, TDS2024B) and current amplifier. During the measurement, a set of neutral density filters were used to control the light intensity (100%, 50%, 25%, and 10%). The results indicate that the p-BVO photoanode exhibits much faster electron transport, indicating the enhancement of the charge separation/transport efficiency in the p-BVO.

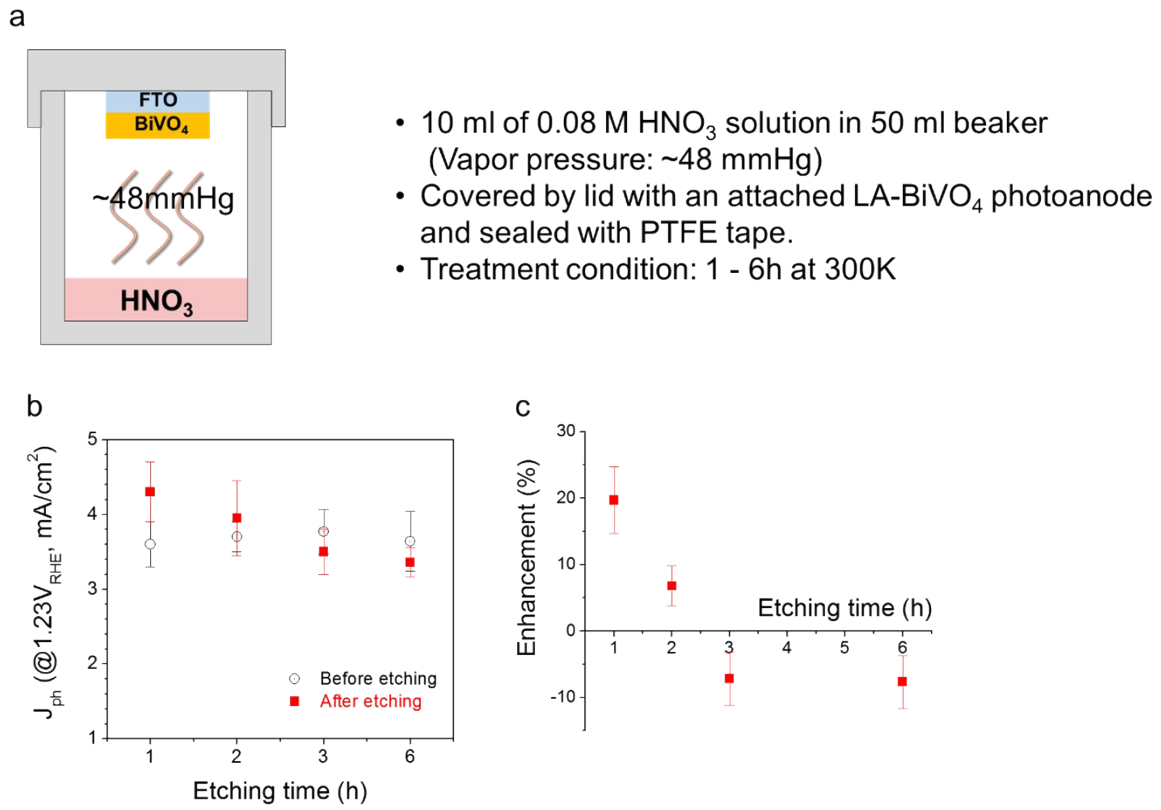

Fig. S22 HNO_3 vapor etching setup, experimental conditions, and determination of optimal etching time. (a) Etching setup and experimental conditions. (b) Photocurrent density and (c) charge transfer efficiency variations as a function of etching time. Etching time of 1 h gives a highest enhancement. Longer than 1 h reduces the photocurrent density severely, which is due to the excessive etching of the p-BVO.

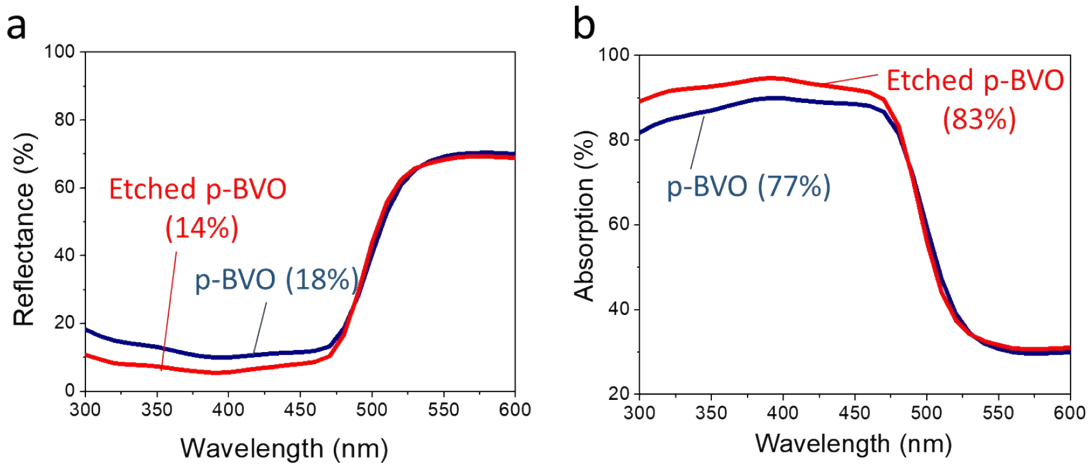

Fig. S23 Effects of HNO_3 vapor etching on light reflectance and absorption of the p-BVO photoanode. (a) Reflectance spectra (b) Absorption before/after nitric acid vapor etching. The surface etching reduces the integrated reflectance from 18 to 14 % in the wavelength range of 300-520 nm, thereby improving the overall light absorption from 77% to 83%. Values shown in parentheses are integrated reflectance and absorption values (300-520 nm).

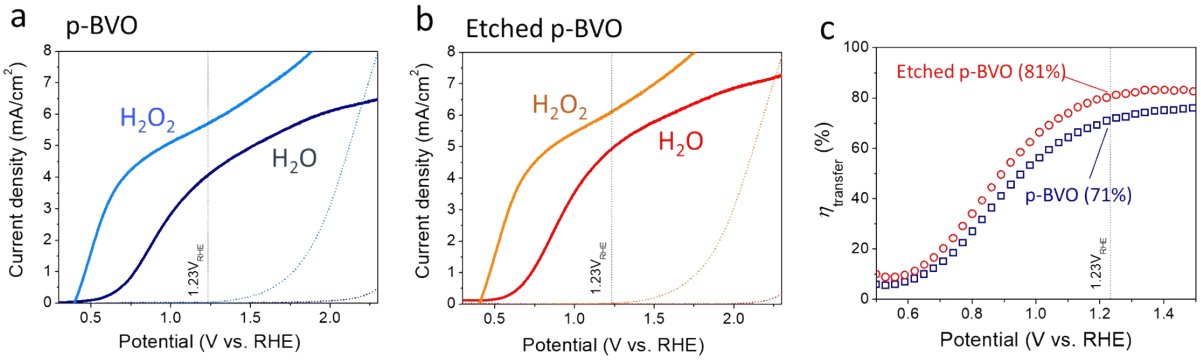

Fig. S24 Effects of surface etching on the charge transfer efficiency. J-V curves of (a) p-BVO and (b) Etched, p-BVO photoanodes in water and H_2O_2 hole scavenger. (c) Charge transfer efficiencies of p-BVO and Etched p-BVO photoanodes. After the surface etching (1h), the charge transfer efficiency increased ~14%, which is attributed to the increased surface area by the surface patterning.

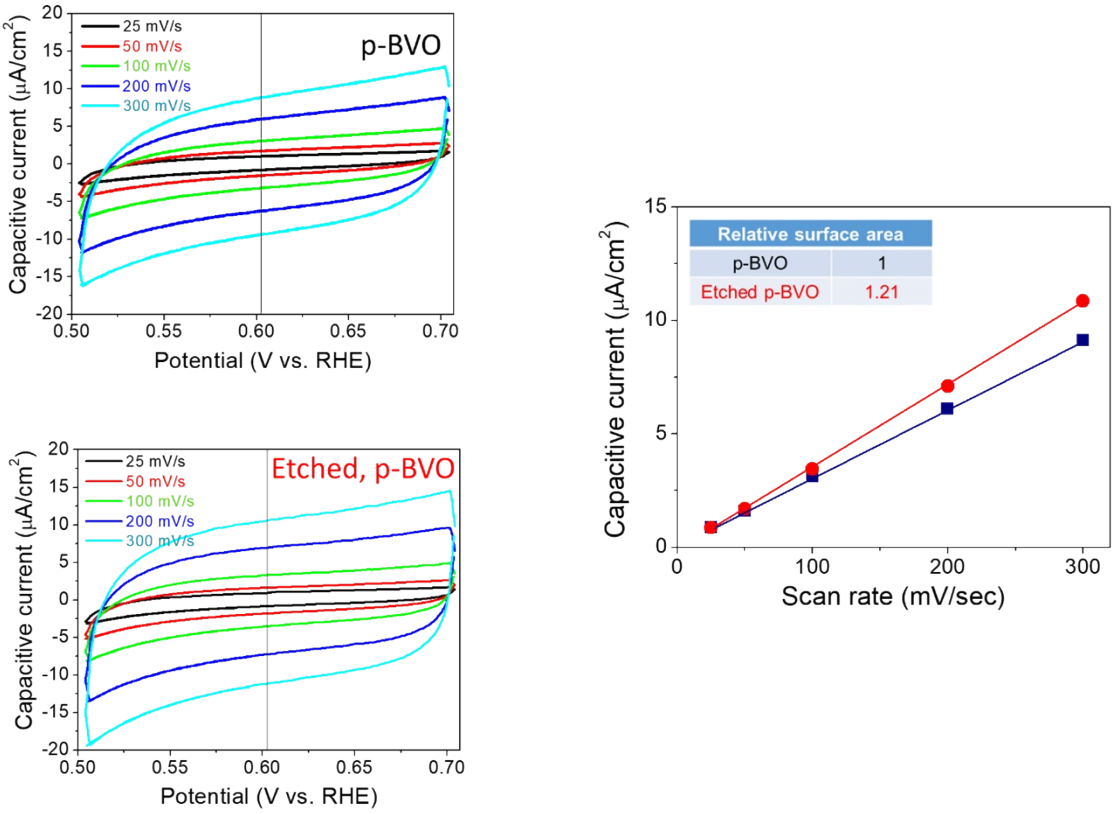

Fig. S25 Effects of surface etching on the relative surface area. (a) Cyclic voltammetry (C-V) curves of (a) p-BVO and (b) Etched, p-BVO photoanodes measured at different scan rates (25-300 mV/sec). (c) Comparison of relative electrochemical surface area of p-BVO and Etched, p-BVO photoanodes. After the surface etching (1h), relative electrochemical surface area increased ~20%.

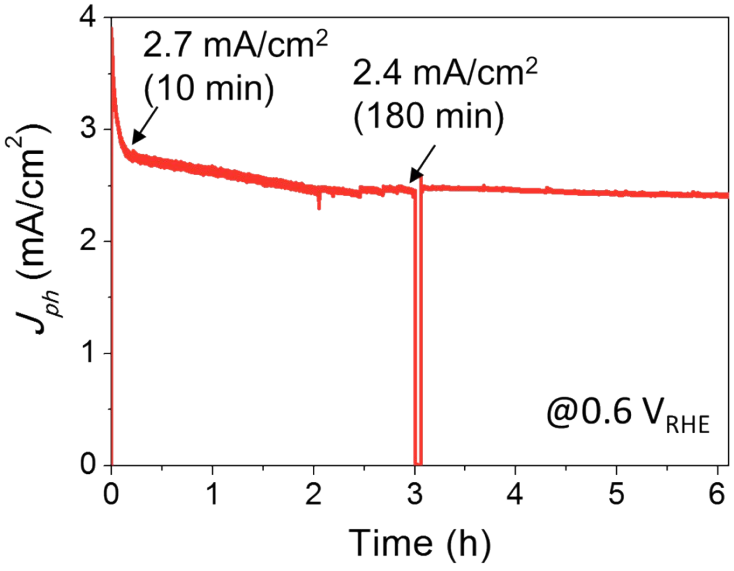

Fig. S26 Photocurrent density vs. time (J-t) curves (two electrode) measured at 0.6 V_{RHE} in 0.5 M phosphate buffer electrolyte (pH 7.0) with stirring (to remove O_2 bubbles trapped on the surface) for 6 h. After the first 10 min, the Co-pi/etched p-BVO photoanode shows relatively stable photocurrent density (~2.4 mA/cm^2, ~11% degradation for 6 h).

Table S1. Statistical data on photocurrent density values (@1.23 V_{RHE}) of (a) p-BVO and (b) r-BVO photoanodes.

a **p-$BiVO_4$**

Thickness	**Photocurrent density** (mA/cm^2, at 1.23 V_{RHE})						
(nm)	Sample 1	Sample 2	Sample 3	Sample 4	Sample 5	Mean	Std D
200	0.7375	0.7123	0.8553	0.6069	0.6299	0.70838	0.09862
550	3.3468	3.3921	3.3281	3.1573	3.2307	3.291	0.09516
800	3.8656	3.6541	3.8971	3.9489	3.9173	3.8566	0.11719
1500	2.7749	2.8693	2.9672	2.9785	3.029	2.92378	0.10135

b **r-$BiVO_4$**

Thickness	**Photocurrent density** (mA/cm^2, at 1.23 V_{RHE})				
(nm)	Sample 1	Sample 2	Sample 3	Mean	Std D
160	0.58637	0.7243	0.79067	0.70045	0.10421
310	0.5215	0.3599	0.598	0.49313	0.12156
540	0.3912	0.2298	0.3499	0.32363	0.08384
800	0.08125	0.03949	0.16916	0.09664	0.06619

Table S2. Electrochemical impedance spectroscopy (EIS) analysis results of the p-BVO and r-BVO photoanodes. The R1, R2 and R3 resistance values are extracted from fitting.

Samples	R_1 (Ohm)	R_2 (Ohm)	R_3 (Ohm)
p-BVO	22.6	79.1	711
r-BVO	21.0	110.1	8552.0

Table S3. Reported performance of $BiVO_4$-based photoanodes without oxygen evolution catalyst.

Reference		Photoanode	Electrolyte (pH)	J_{ph}@1.23V_{RHE} (mA/cm^2)
Pristine $BiVO_4$	This work	p-BVO	0.5 M phosphate buffer solution (pH 7)	**3.9**
	This work	Etched p-BVO	0.5 M phosphate buffer solution (pH 7)	**4.9**
	Ref 1.	Photocharged BVO	0.1 M phosphate-borate-acetate buffer (pH7)	3.3
			0.1 M Na_2SO_4 (pH 7)	1.5
	Ref 2.	Electrochemically treated BVO (E-BVO)	1 M potassium borate (pH 9.5)	2.5
	Ref 3.	Hydrogen-treated BVO	0.5 M Na_2SO_4 aqueous solution (pH 6.8)	2.5
Doped $BiVO_4$	Ref 4.	Gradient-doped W:BVO	0.1M potassium phosphate (pH ~7.3)	1.1
	Ref 5.	H_2-treated Mo:BVO	0.1 M bicarbonate (pH 7.0)	2.6
	Ref 6.	Mo:BVO	0.1 M Na_2SO_4 aqueous solution (pH 6.6)	2.4
		W:BVO		2.0
Nano- or Hetero-Structured $BiVO_4$	Ref 7.	N_2-treated nanoporous BVO	0.5M phosphate buffer solution (pH 7.2)	2.8
	Ref 8.	W,Mo:BVO/Helix WO_3	0.5M K_2SO_4 /w phosphate buffer (pH 7)	3.9

Table S4. Reported performance of $BiVO_4$-based photoanodes with oxygen evolution catalyst.

Reference		Photoanode	Electrolyte (pH)	J_{ph}@0.6V_{RHE} (mA/cm^2)	J_{ph}@1.23V_{RHE} (mA/cm^2)
Pristine $BiVO_4$	This work	Co-Pi/Etched p-BVO	0.5M phosphate buffer solution (pH 7)	3.5	6.1
	Ref 2.	CoBi/Electrochemically treated BVO	1 M potassium borate (pH 9.5)	1.6	3.2
Doped $BiVO_4$	Ref 4.	Co-Pi/Gradient-doped W:BVO	0.1M potassium phosphate (pH ~7.3)	2.0	3.6
	Ref 5.	Co-Pi/H_2-treated Mo:BVO	0.1M phosphate buffer (pH 7)	2.3	5.0
Nano- or Hetero-Structured $BiVO_4$	Ref 7.	NiOOH/FeOOH/ N_2-treated BVO	0.5M phosphate buffer solution (pH 7.2)	3.5	5.1
	Ref 8.	NiOOH/FeOOH/ W,Mo:BVO/Helix WO_3	0.5M K_2SO_4 /w phosphate buffer (pH 7)	3.1	5.4

References

1. Trzesniewski, B. J. *et al.* Near-complete suppression of surface losses and total internal quantum efficiency in $BiVO_4$ photoanodes. *Energy Environ. Sci.* **10**, 1517-1529 (2017)
2. Wang, S. *et al*. Electrochemically-Treated BiVO4 Photoanode for Efficient Photoelectrochemical Water Splitting. *Angew. Chem. Int. Ed*. **56**, 8500–8504 (2017)
3. Wang, G. *et al*. Computational and Photoelectrochemical Study of Hydrogenated Bismuth Vanadate. *J. Phys. Chem. C.* **117**, 10957−10964 (2013)
4. Abdi, F. F. *et al.* Efficient solar water splitting by enhanced charge separation in a bismuth vanadate-silicon tandem photoelectrode. *Nat. Commun.* **4**, 2195. (2013)
5. Kim, J. H. *et al.* Wireless solar water splitting device with robust cobalt-catalyzed, dual-doped $BiVO_4$ photoanode and perovskite solar cell in tandem: a dual absorber artificial leaf. *ACS nano*. **9**(12), 11820-11829. (2015)
6. Parmar, K. P. S. *et al.* Photocatalytic and Photoelectrochemical Water Oxidation over Metal-Doped Monoclinic $BiVO_4$ Photoanodes. *ChemSusChem*, **5**(10), 1926-1934. (2012)
7. Kim, T. W. *et al.* Simultaneous enhancements in photon absorption and charge transport of bismuth vanadate photoanodes for solar water splitting. *Nat. Commun*. **6**, 8769 (2015).
8. Shi, X. *et al.* Efficient photoelectrochemical hydrogen production from bismuth vanadate-decorated tungsten trioxide helix nanostructures. *Nat. Commun.* **5**, 4775 (2014).